



Article

Experimental and Finite Element Study of Polymer Infilled Tube-in-Tube Buckling Restrained Brace

Robel Wondimu Alemayehu ¹, Youngsik Kim ^{1,2}, Min Jae Park ¹, Manwoo Park ³ and Young K. Ju ^{1,*}¹ School of Civil, Environmental and Architectural Engineering, Korea University, Seoul 02841, Korea; robel@korea.ac.kr (R.W.A.); yskim@techsq.co.kr (Y.K.); alswo8739@korea.ac.kr (M.J.P.)² Technical Research Center, TechSquare Co., Ltd., Seoul 06710, Korea³ KG Dongbu Steel, Seoul 04637, Korea; imwpark@kggroup.co.kr

* Correspondence: tallsite@korea.ac.kr

Abstract: This study presents a tube-in-tube buckling-restrained brace (BRB) infilled with lightweight and rapid hardening polymer. The proposed BRB consists of a circular or square tube core encased with a tube of similar shape and polymer infill. The tube-in-tube arrangement minimizes the filler material volume and enables the use of rolled steel section as opposed to welded profiles commonly utilized when large BRB axial strength is required, although welded profiles suffer from low assembly accuracy resulting from welding deformation. The infilled polymer has a density of approximately half that of mortar and requires a curing time of 24 h, enabling weight and fabrication time reduction. The stability and inelastic deformation capability of the BRB were investigated through brace and subassembly tests of six circular and four-square full-scale specimens, followed by finite element analysis. The test results show that circular BRB designed with a P_{cr}/P_y ratio of 1.46 exhibited a stable hysteresis up to 1.42% and 1.06% core strain in tension and compression, respectively. Circular and square specimens designed with P_{cr}/P_y ratios ranging from 0.82 to 1.06 exhibited stable hysteresis before failing by global buckling at compressive core strains ranging from 0.86% to 1.09%. The slot weld detail adopted for welding core projection stiffener displayed a stable performance in circular BRB specimens, while it resulted in large plastic strain demand in square BRB specimens, leading to core fracture at tensile core strains ranging from 0.64% to 0.71%.

Keywords: buckling-restrained brace; subassembly test; component test; finite element analysis; polymer infilled BRB; slot weld



Citation: Alemayehu, R.W.; Kim, Y.; Park, M.J.; Park, M.; K. Ju, Y. Experimental and Finite Element Study of Polymer Infilled Tube-in-Tube Buckling Restrained Brace. *Metals* **2021**, *11*, 1358. <https://doi.org/10.3390/met11091358>

Academic Editor: Giovanni Meneghetti

Received: 30 July 2021

Accepted: 23 August 2021

Published: 29 August 2021

Publisher's Note: MDPI stays neutral with regard to jurisdictional claims in published maps and institutional affiliations.



Copyright: © 2021 by the authors. Licensee MDPI, Basel, Switzerland. This article is an open access article distributed under the terms and conditions of the Creative Commons Attribution (CC BY) license (<https://creativecommons.org/licenses/by/4.0/>).

1. Introduction

Buckling-restrained braces (BRBs) have been widely utilized to enhance the seismic performance of new and existing buildings as well as for post-earthquake retrofitting [1–6]. BRBs differ from conventional braces because the BRB core yields under both tension and compression without buckling. Numerous BRB types have been proposed and tested [7–11]. A typical BRB consists of a steel core encased by a steel tube filled with mortar or concrete. A thin layer of debonding material or a small gap separates the steel core and infilled material. Hence, the core sustains axial tension and compression without buckling under the restraining effect of the casing and filler material. The long curing time and high density of concrete/mortar negatively affect the fabrication time and dead-weight of such BRBs. To address these drawbacks, and in a few cases to allow disassembly and inspection, several all-steel BRBs, including flat, cruciform, and H-section core BRBs, have been proposed and tested [12–15]. When large BRB axial strength is required, cruciform, H-section, or other core profiles are better alternatives to a thick flat plate core. However, core cross-sections assembled by welding multiple steel plates have low fatigue life and assembly accuracy, owing to welding deformation and residual stress [16].

This paper proposes polymer infilled tube-in-tube BRBs to eliminate the drawbacks of concrete/mortar-filled BRBs. Moreover, they utilize rolled steel sections to avoid defects

that arise from the use of sections assembled by welding. The proposed BRB consists of a circular or square hollow section core encased by a larger hollow section of the same shape, as illustrated in Figure 1. The gap between the core and the casing is filled with a rapid-hardening lightweight polymer material produced by a chemically reacting diisocyanate and polyol mixture [17]. The development of polymer composites and engineered materials for structural application has been gaining popularity in the past few decades [17,18]. The infilled polymer is initially a yellowish-brown viscous fluid; it solidifies gradually and fully hardens within 24 h at room temperature. The polymer has a density of 1178 kg/m^3 (about half that of mortar) in its hardened state [17]. The adequacy of the polymer for structural use in steel–polymer hybrid floor systems has been demonstrated [17].

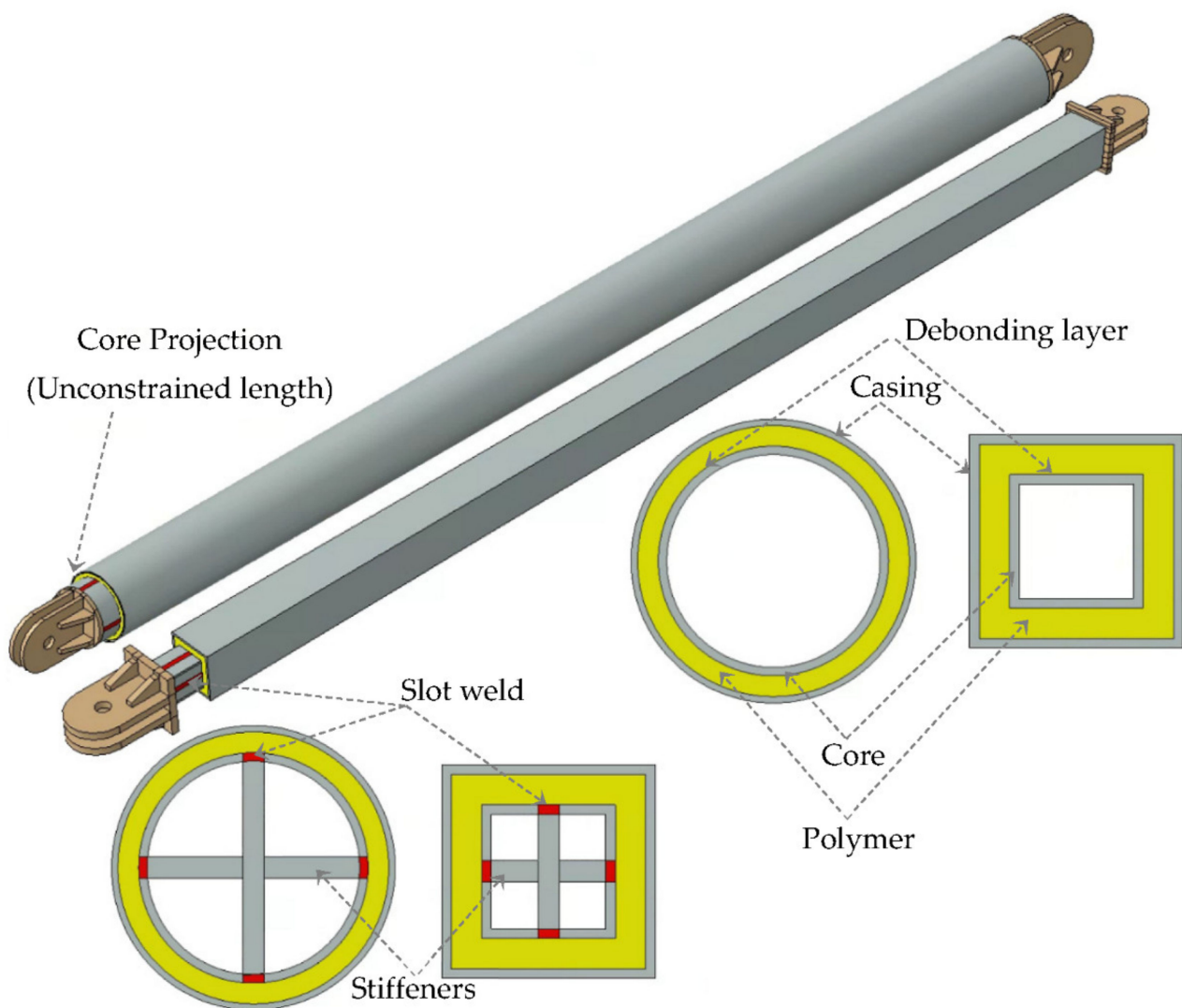


Figure 1. Polymer infilled tube-in-tube buckling-restrained brace.

The unconstrained segment of the core projecting out of the casing is subjected to large in-plane bending and prone to failure [19,20]. To minimize the number of such potential failure zones, the core projection is only on one end of the proposed BRB, as opposed to two ends such as in a conventional BRB. The core projection is stiffened, as shown in Figure 1.

Ten full-scale specimens were tested under brace and subassembly cyclic load tests. The test program investigated the buckling behavior and unconstrained length stiffener detail of the BRB. Nonlinear finite element analysis [21–23] was conducted to better understand the proposed BRB.

2. Test Program

2.1. Test Specimens

The test program consists of six circular and four square tube-in-tube full-scale specimens with varying stiffness and strength parameters. Figure 2 and Table 1 summarize the details of the test specimens fabricated using SRT275 and SJT275 steel, with a specified minimum yield strength of 275 MPa. The core of one square BRB specimen was fabricated using SRT 355 steel with a specified minimum yield strength of 355 MPa to examine the behavior of the BRB under different steel grades. The stiffeners and pin connectors at the BRB ends were fabricated using SM355 steel, with a specified minimum yield strength of 355 MPa. The average material properties with the respective coefficient of variation obtained from three coupon tests conducted on the components of the specimens are reported in Table 2. The yield strength obtained from the coupon test was higher than the specified nominal strength by a factor of 1.6 and 1.4 for circular and square specimens, respectively. The specimen and component (core and casing) names in Tables 1 and 2 represent the respective shapes and sizes. C and S denote circular and square tubes, respectively, followed by the outside diameter or width of the tube and wall thickness in millimeters. For example, C216 t8 indicates a circular tube with 216 mm diameter and 8 mm wall thickness. The specimen names indicate the core size, followed by the casing size. The first two circular specimens were identical except for core wall thickness, while the third circular specimen was more slender compared to the first two. Similarly, the first two square specimens were identical except for core wall thickness and steel grade, while the third square specimen was more slender compared to the first two.

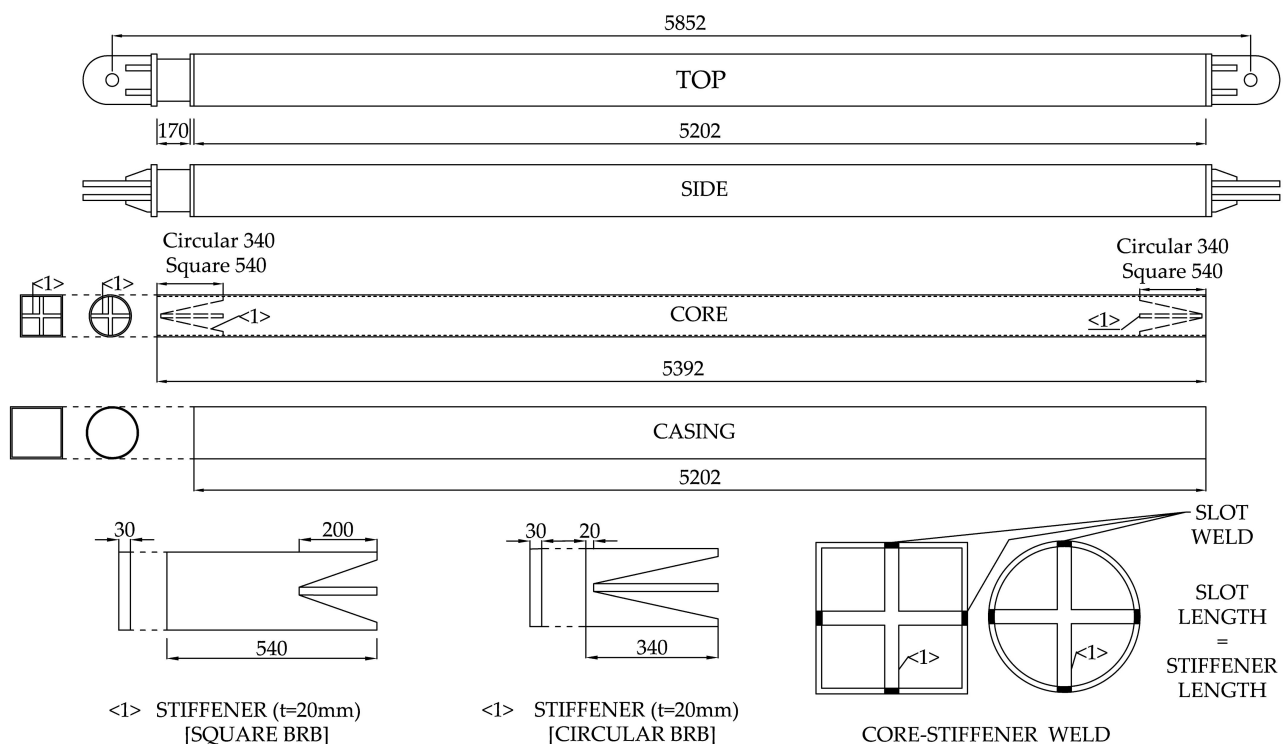


Figure 2. Details of the proposed BRB. (All dimensions are in mm).

The infilled polymer, in its fully hardened state, has density, tensile strength, compressive strength, modulus of elasticity in tension, and modulus of elasticity in compression of 1178 kg/m³, 31.4 MPa, 23.1 MPa, 1277 MPa, and 461 MPa, respectively. To minimize friction and achieve a similar force strength in tension and compression, a 1.6 mm thick rubber was applied as a debonding layer between the core and infilled polymer [24].

Using the mechanical properties obtained from the coupon test, the global stability of the test specimens was estimated using Euler's buckling theory. The critical buckling load

(P_{cr}) and the bending moment at the center of the casing (M_{center}) [25,26] were calculated using Equations (1) and (2), respectively.

$$P_{cr} = \frac{\pi^2 EI}{L^2} \quad (1)$$

$$M_{center} = \frac{P\nu_0}{1 - \frac{P}{P_{cr}}} \quad (2)$$

where E , I , and L represent the modulus of elasticity, casing moment of inertia, and effective brace length, respectively. The modulus of elasticity was taken as 200 GPa for all specimens. To estimate the brace stability, P_{cr} was compared with the brace yielding force P_y , and ultimate force P_u , computed as the product of the core cross-sectional area, with the yield and ultimate stress, respectively. Watanabe et al. [27] recommended a P_{cr}/P_y ratio above 1.5 to provide sufficient constraint against global buckling. Moreover, flexural yielding of the casing should be prevented to avoid global buckling [14]. Thus, the casing moment (M_{center}) computed by Equation (2) was compared with the casing yield moment, (M_y) calculated as the product of the casing elastic section modulus and the casing yield strength. Here, P and ν_0 are the brace axial force and brace initial imperfection amplitude, respectively. The initial imperfection was taken as 12 mm ($L/500$) [28]. For convenient comparison of P with M_{center} and M_y , P_{cy} in Equation (3) was defined as the brace axial force corresponding to casing flexural yield and computed by equating M_{center} to M_y in Equation (2). The computed strength and stiffness parameters are listed in Table 3.

$$P_{cy} = \frac{M_y}{\nu_0 + \frac{M_y}{P_{cr}}} \quad (3)$$

Table 1. Test specimens.

| Specimen | Shape | Number of Specimens | Core ¹ | | Casing ¹ | | Polymer Thickness (mm) |
|-----------------|----------|---------------------|-------------------|------------|---------------------|------------|------------------------|
| | | | Size ¹ | Steel Type | Size ¹ | Steel Type | |
| C216 t8–C267 t6 | Circular | 4 | 216.3 t8 | SRT275 | 267.4 t6 | SJT275 | 17.95 |
| C216 t6–C267 t6 | | 1 | 216.3 t6 | SRT275 | 267.4 t6 | SRT275 | 17.95 |
| C165 t7–C216 t6 | | 1 | 165.2 t7 | SRT275 | 216.3 t6 | SRT275 | 17.95 |
| S125 t9–S200 t9 | Square | 2 | 125 t9 | SRT275 | 200 t9 | SRT275 | 26.90 |
| S125 t7–S200 t9 | | 1 | 125 t7 | SRT335 | 200 t9 | SRT275 | 26.90 |
| S100 t9–S175 t6 | | 1 | 100 t9 | SRT275 | 175 t6 | SRT275 | 29.90 |

¹ Outside tube diameter/width followed by wall thickness.

Table 2. Material properties.

| Component | Steel Type | Yield Strength | | Ultimate Strength | | Elongation | |
|-------------------------|------------|----------------|---------------------|-------------------|---------------------|-------------|---------------------|
| | | Average (MPa) | CV ³ (%) | Average (MPa) | CV ³ (%) | Average (%) | CV ³ (%) |
| C267 t6 | SJT275 | 422 | 1.25 | 486 | 0.75 | 20.8 | 5.69 |
| C216 t8 | SRT275 | 437 | 0.35 | 476 | 0.59 | 16.8 | 6.33 |
| C216 t6 | SRT275 | 418 | 1.65 | 461 | 1.38 | 20.1 | 6.38 |
| C165 t7 | SRT275 | 441 | 1.06 | 475 | 0.56 | 16.1 | 9.12 |
| S175 t6 | SRT275 | 329 | 0.47 | 421 | 0.46 | 23.0 | 4.58 |
| S125 t9 | SRT275 | 386 | 0.79 | 423 | 0.80 | 18.1 | 6.33 |
| S125 t7 | SRT355 | 525 | 1.98 | 575 | 1.97 | 12.5 | 9.59 |
| S100 t9 | SRT275 | 377 | 1.33 | 426 | 1.66 | 16.0 | 5.24 |
| Stiffener ¹ | SM355 | 349 | 1.52 | 524 | 0.84 | 25.9 | 3.85 |
| Pin plates ² | SM355 | 397 | 1.87 | 534 | 0.23 | 26.9 | 1.53 |

¹ 20 mm thick. ² 30 mm thick. ³ Coefficient of variation.

Table 3. Strength and stiffness parameters.

| Specimen | Core | | Casing | | | | |
|-----------------|------------|------------|---------------|--------------|-----------------------|--------------|--------------|
| | P_y (kN) | P_u (kN) | P_{cr} (kN) | M_y (kN.m) | P_{cy} ¹ | P_{cr}/P_y | P_{cy}/P_y |
| C216 t8–C267 t6 | 2289 | 2494 | 2427 | 133 | 1991 | 1.06 | 0.87 |
| C216 t6–C267 t6 | 1659 | 1826 | 2427 | 133 | 1991 | 1.46 | 1.20 |
| C165 t7–C216 t6 | 1534 | 1652 | 1264 | 85 | 1072 | 0.82 | 0.70 |
| S125 t9–S200 t9 | 1611 | 1765 | 2415 | 162 | 2048 | 1.5 | 1.27 |
| S125 t7–S200 t9 | 1734 | 1899 | 2415 | 162 | 2048 | 1.39 | 1.18 |
| S100 t9–S175 t6 | 1234 | 1396 | 1114 | 73 | 941 | 0.9 | 0.76 |

¹ Brace axial force that results in casing flexural yielding.

2.2. Test Setup

The BRB specimens were subjected to cyclic load through a 3000 kN actuator in the brace and subassembly setups, as illustrated in Figure 3. In the brace test setup, which subjects the specimens to axial tension and compression, the specimens were constrained at one end through a pin support connected to a reaction block and pin-connected to the actuator at the opposite end. The movement of the actuator was constrained to be in the axial direction of the test specimen through a guide frame and a set of rollers, as illustrated in Figure 3a. In the subassembly test setup, the BRB specimens were inclined at an angle of 33.69° and pin-connected to the column, as illustrated in Figure 3b, resulting in a 4 m story height and 6 m bay width configuration. The column base and the opposite end of the BRB specimen were pin-connected to the strong floor. The out-of-plane movement of the column was restrained by a lateral support frame and a set of rollers, as illustrated in Figure 3b. One of the four C216 t8–C267 t6 and one of the two S125 t9–S200 t9 BRB specimens were tested in the subassembly setup, while the other specimens were tested in the brace test setup.

2.3. Instrumentation

The brace's axial deformation was monitored through displacement transducer 1, attached as illustrated in Figure 3. Moreover, the in-plane vertical and out-of-plane horizontal displacement of the BRB was monitored through displacement transducers 2 and 3, respectively, attached at the mid-length of the BRB. In addition, longitudinal and tangential strain components at the end of the stiffeners and BRB mid-length were monitored through strain gauges 1 to 10, arranged as illustrated in Figure 4. Strain gauges 1, 3, 4, 7, and 9 were adopted to measure longitudinal strain components, while strain gauges 2, 5, 6, 8, and 10 were adopted to measure tangential strain components.

2.4. Loading Protocol

The quasi-static cyclic loading protocol adopted from AISC seismic provision [29] and applied in the test is illustrated in Figure 5. The loading protocol starts with two cycles of loading, at Δ_{by} loading amplitude, followed by two cycles of $0.5\Delta_{bm}$, $1.0\Delta_{bm}$, $1.5\Delta_{bm}$, and $2.0\Delta_{bm}$. Here, Δ_{by} and Δ_{bm} indicate brace deformation at core yielding and design story drift, respectively [29]. Δ_{bm} indicates displacement amplitude at the design story drift and was set to be 1.0% of the story height [29], and Δ_{by} represents brace-yielding displacement. Following the $2.0\Delta_{bm}$ cycle, the loading protocol continues with fatigue loading at $1.5\Delta_{bm}$ loading amplitude until the cumulative plastic deformation exceeds $200\Delta_{by}$ [29]. The fatigue loading is only required for the brace test setup [29].

The brace's axial deformation (δ) and the story drift (d) were related by Equation (4). L and L_B are as defined in Figure 6. The brace's axial deformation (δ) was monitored through displacement transducer 1 in all the tests. d and δ corresponding to $2.0\Delta_{bm}$ were 80 mm and 66.56 mm, respectively, for the 4 m by 6 m subassembly utilized in the test.

$$\delta = \frac{L \times d}{L_B} \quad (4)$$

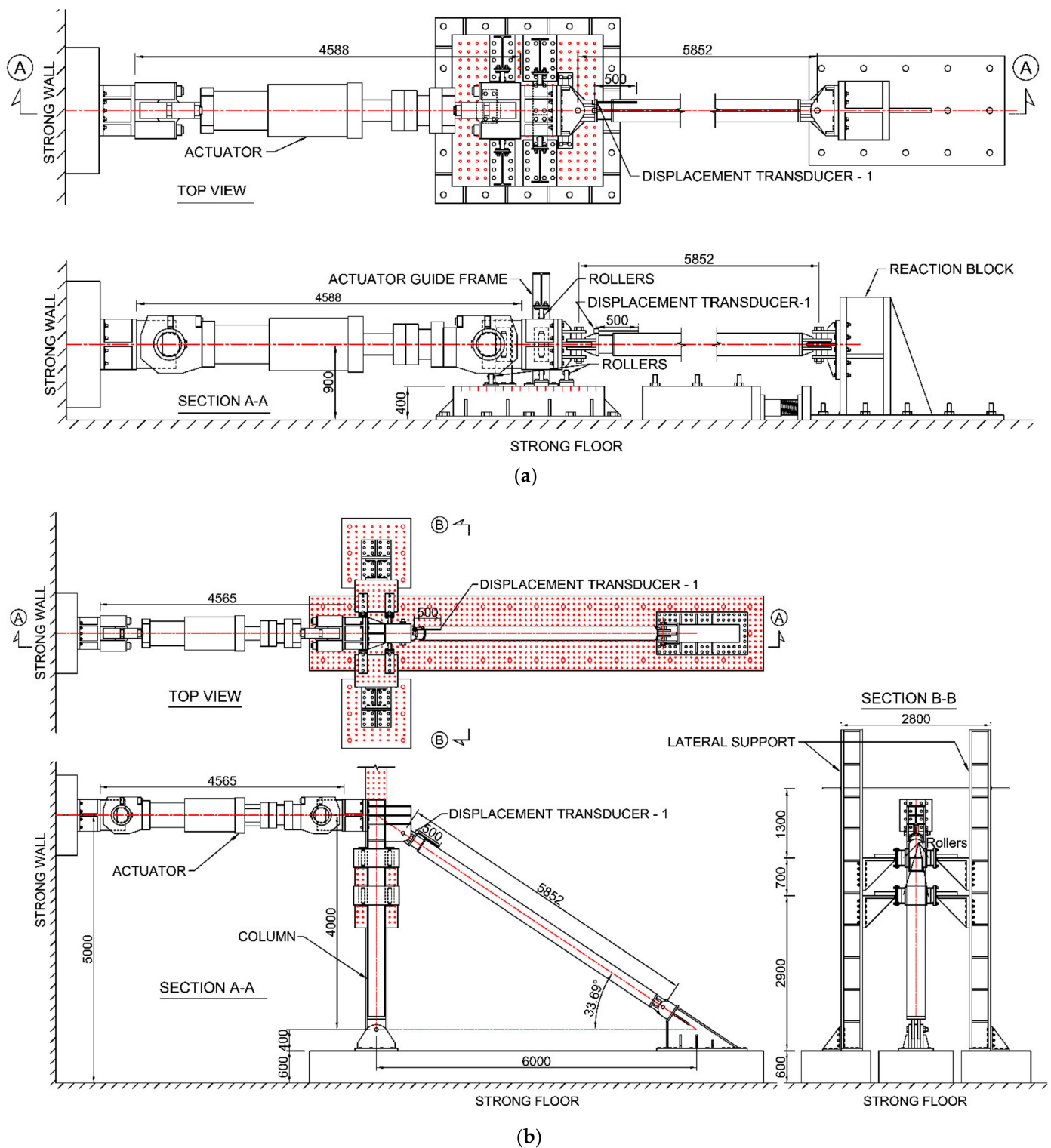


Figure 3. Test setup. (a) Brace test; (b) subassembly test. (All dimensions are in mm).

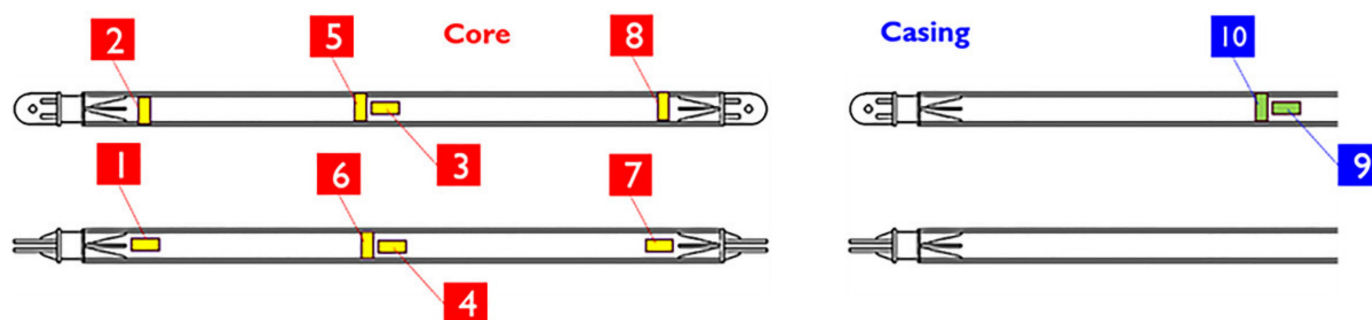


Figure 4. Strain gauge arrangement, orientation, and numbering.

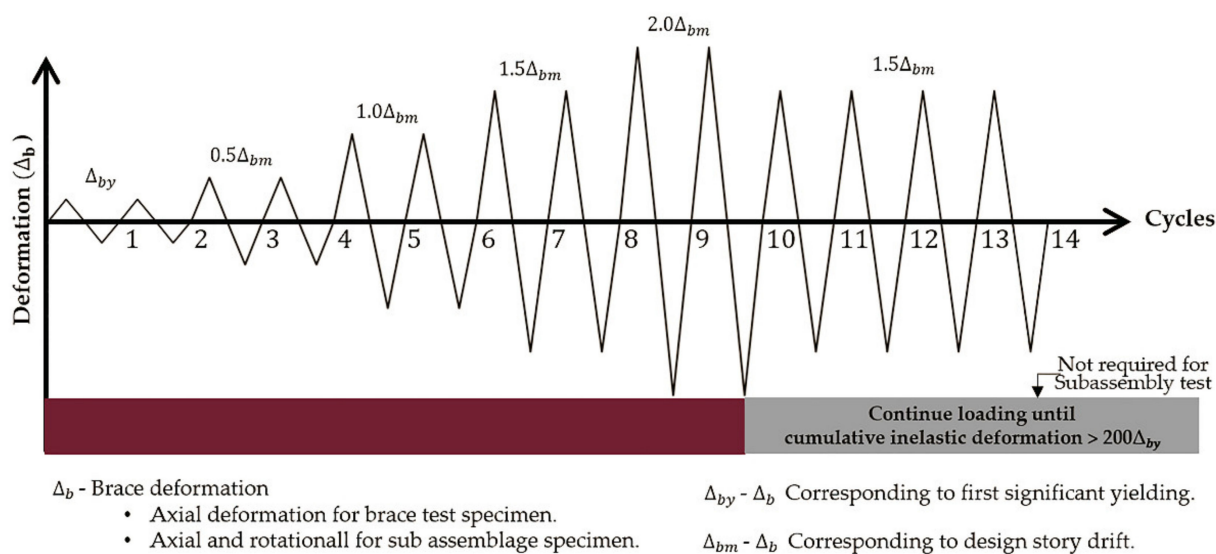


Figure 5. Loading protocol.

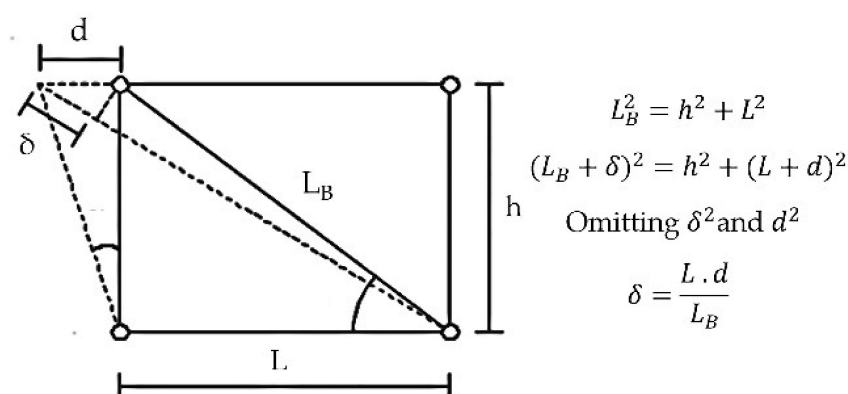


Figure 6. Brace axial deformation and story drift correlation.

3. Test Results

3.1. Circular Specimens

Figure 7 illustrates the brace's axial deformation (δ), measured by displacement transducer 1 versus the applied force. Compressive force and displacement are indicated on the positive axis. To distinguish in which test setup the specimens were tested, "B" and "S" were added at the end of the specimen names to indicate brace and subassembly test setups, respectively. C216 t8–C267 t6-B1, C216 t8–C267 t6-B2, and C216 t8–C267 t6-B3 represent the three specimens of C216 t8–C267 t6 tested in the brace test setup.

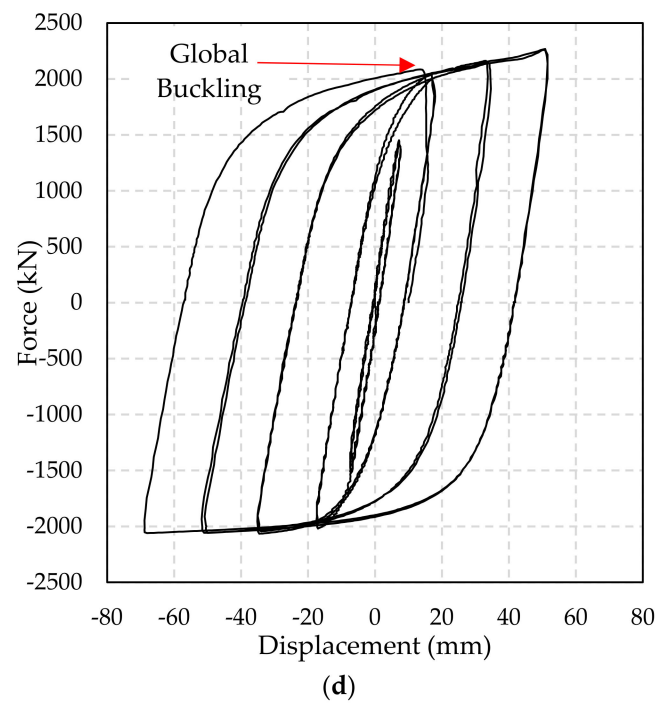
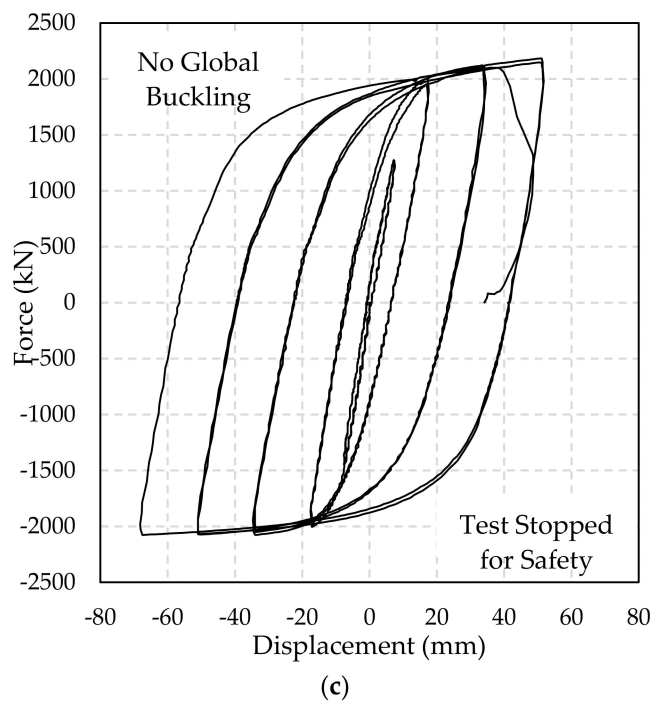
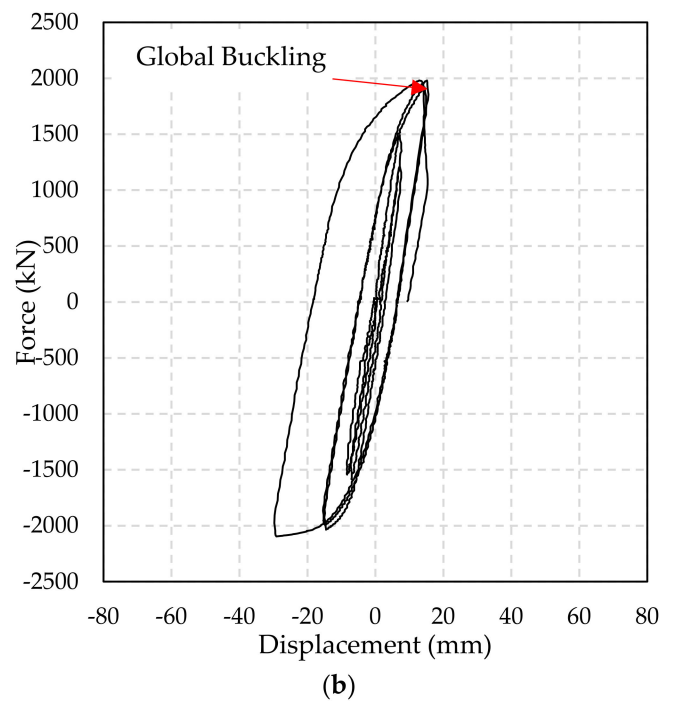
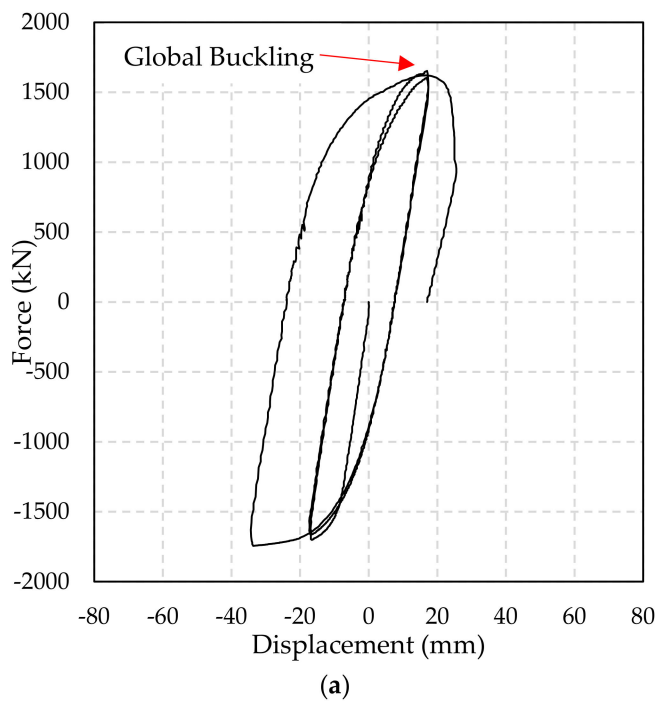


Figure 7. Cont.

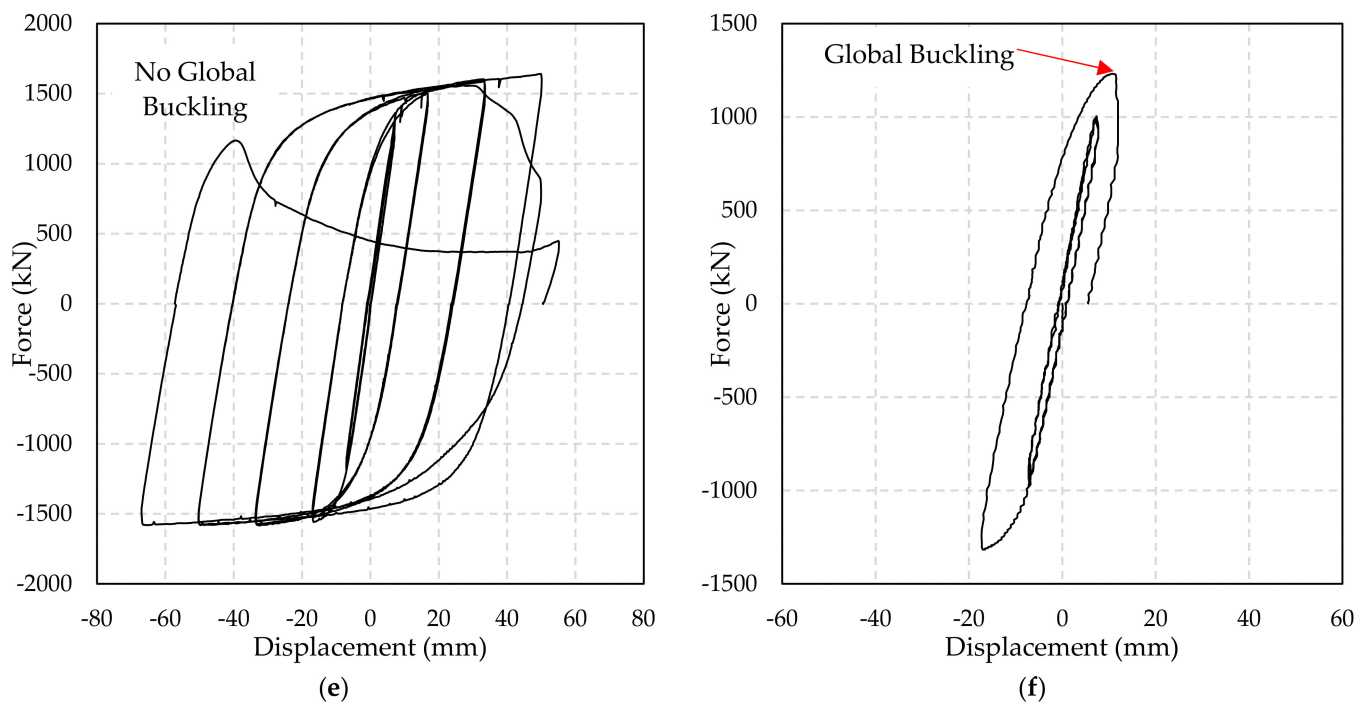


Figure 7. Hysteretic response of circular specimens: (a) C216 t8–C267 t6-S; (b) C216 t8–C267 t6-B1; (c) C216 t8–C267 t6-B2; (d) C216 t8–C267 t6-B3; (e) C216 t6–C267 t6-B; (f) C165 t7–C216 t6-B.

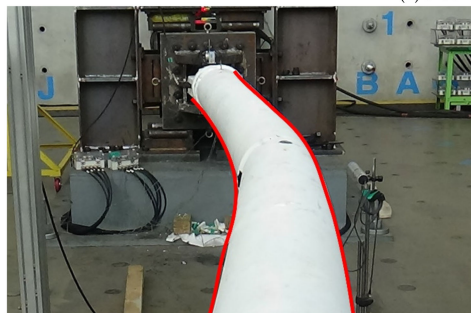
As illustrated in Figures 7 and 8, and summarized in Table 4, all the C216 t8–C267 t6 specimens tested in the brace and subassembly test setup failed by global buckling except C216 t8–C267 t6-S-B2, where the test was terminated for safety. Among the C216 t8–C267 t6 specimens, C216 t8–C267 t6-S and C216 t8–C267 t6-B1 failed prematurely at the first compressive loading of the $1.0\Delta_{bm}$ cycle, while C216 t8–C267 t6-B2 and C216 t8–C267 t6-B3 exhibited stable hysteresis up to the first compressive loading of the $2.0\Delta_{bm}$ cycle, achieving a maximum core strain of 1.46% and 1.10% in tension and compression, respectively. Similarly, the C216 t6–C267 t6-B specimen, which had the highest P_{cr}/P_y ratio among the circular specimens, did not fail by global buckling and exhibited a stable hysteresis up to a core strain of 1.42% in tension and 1.06% in compression. As illustrated in Figure 7e, C216 t6–C267 t6-B exhibited stable hysteresis until compressive strength loss occurred in the second $1.5\Delta_{bm}$ loading cycle without any visible damage or global buckling, as illustrated in Figure 8d. Loading was continued to the next loading step, and the specimen exhibited a stable response up to 1.42% core strain in tension. However, its strength deteriorated in the next compressive loading step without global buckling or noticeable damage. To investigate the cause of failure, and inspect the core while preserving the polymer infill, specimen C216 t6–C267 t6-B was cut by a water jet. As illustrated in Figure 9, there was no local buckling or other defects on the core.

Specimen C165 t7–C216 t6-B, with the lowest P_{cr}/P_y ratio among the circular specimens, failed by global buckling at the first compressive loading of the $0.5\Delta_{bm}$ loading cycle. At the onset of global buckling, P_{max}/P_{cr} and P_{max}/P_{cy} were 0.97 and 1.15, respectively. In the C216 t8–C267 t6 specimens, global buckling occurred at P_{max}/P_{cr} and P_{max}/P_{cy} ratios ranging from 0.82 to 0.93 and 0.99 to 1.14, respectively. In specimen C216 t6–C267 t6, where global buckling was not observed, the maximum axial compressive load was 68% and 82% of P_{cr} and P_{cy} , respectively.

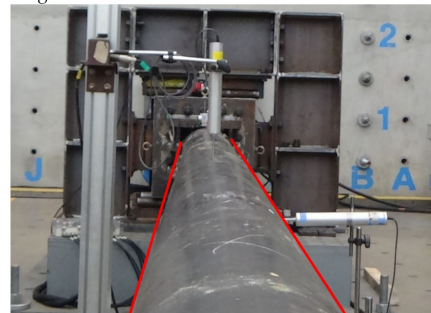
Figure 10 illustrates the typical longitudinal casing strain, measured at the center of the BRB specimens with and without global buckling. Evident from the graphs, the casing provided sufficient restraint against global buckling until yielding occurred. Similar test results have been reported by Alemayehu et al. [14].



(a)Global Buckling



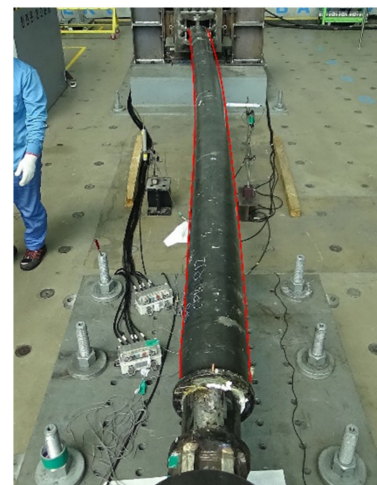
(b)Global Buckling



(c)No Global Buckling, Test Stopped for Safety



(d)No Global Buckling



(e)Global Buckling

Figure 8. Deformed shape at the end of test: (a) C216 t8–C267 t6-S; (b) C216 t8–C267 t6-B1 and C216 t8–C267 t6-B3; (c) C216 t8–C267 t6-B2; (d) C216 t6–C267 t6-B; (e) C165 t7–C216 t6-B.

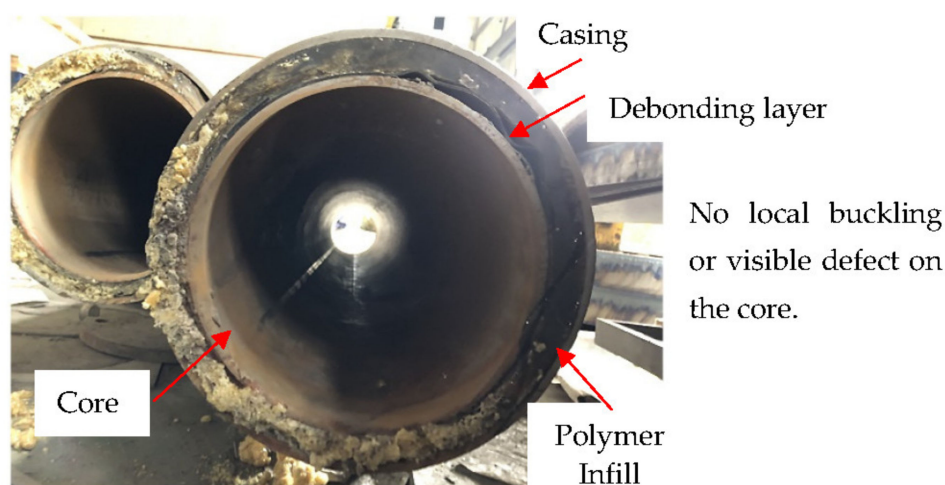
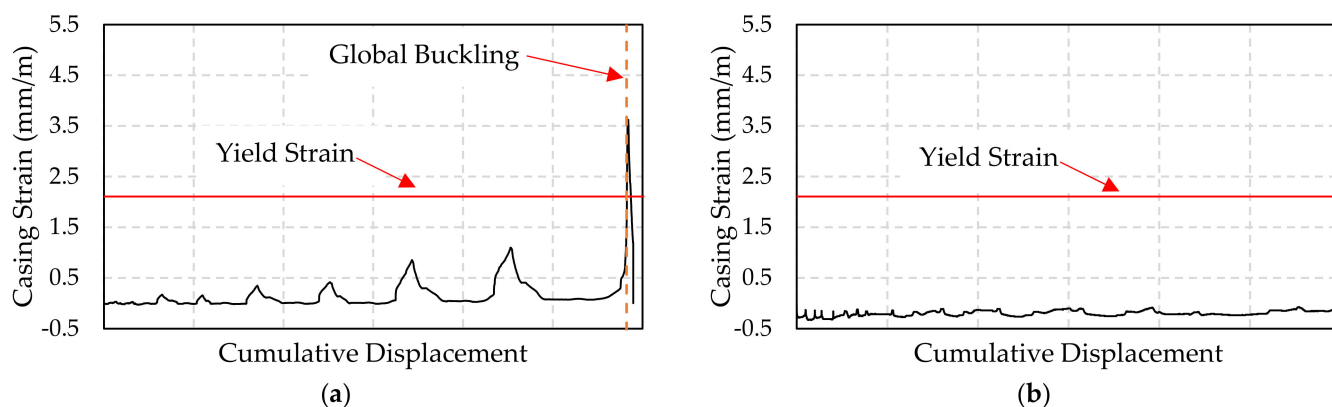
For the core and casing size combination of the tested circular BRBs, global buckling was the governing failure mode. Evident from the casing strain distribution and P_{max}/P_{cy} , global buckling resulted, owing to casing yielding at forces 3–18% lower than P_{cr} .

During all the tests, varying degrees of unsolidified filler material leakage were observed. Such a phenomenon was not present when the filler material was used as part of the composite slab in previous studies [17].

Table 4. Circular specimens test result.

| Specimen | P_{max} (kN) | | δ_{max} (mm) | | ϵ_{max} (%) ³ | | $\frac{P_{max}}{P_{cr}}$ ⁴ | $\frac{P_{max}}{P_{cy}}$ ⁵ | Failure Mode |
|--------------------|-------------------|-------------------|---------------------|------|-----------------------------------|------|---------------------------------------|---------------------------------------|-------------------------|
| | (+) ¹ | (−) ² | (+) | (−) | (+) | (−) | | | |
| C216 t8–C267 t6-S | 1987 ⁶ | 2097 ⁶ | 25.5 | 34.3 | 0.54 | 0.73 | 0.82 | 1.0 | Global buckling |
| C216 t8–C267 t6-B1 | 1980 | 2096 | 15.6 | 29.7 | 0.33 | 0.63 | 0.82 | 0.99 | Global buckling |
| C216 t8–C267 t6-B2 | 2183 | 2078 | 51.8 | 68.2 | 1.10 | 1.45 | 0.90 | 1.10 | Test stopped for safety |
| C216 t8–C267 t6-B3 | 2267 | 2066 | 51.6 | 68.9 | 1.09 | 1.46 | 0.93 | 1.14 | Global buckling |
| C216 t6–C267 t6-B | 1640 | 1584 | 50.1 | 66.9 | 1.06 | 1.42 | 0.68 | 0.82 | No global buckling |
| C165 t7–C216 t6-B | 1231 | 1317 | 11.9 | 17.3 | 0.25 | 0.37 | 0.97 | 1.15 | Global buckling |

¹ Compression. ² Tension. ³ core strain. ⁴ Maximum compressive force to Euler buckling force ratio. ⁵ Maximum compressive force to casing yield force ratio. ⁶ Maximum brace axial force.

**Figure 9.** Cross-section of C216 t6–C267 t6-B after water jet cutting.**Figure 10.** Typical casing longitudinal strain: (a) specimens that failed by global buckling; (b) specimens with no global buckling.

3.2. Square Specimens

Figure 11 illustrates the measured force in the square specimens versus the brace's axial displacement. Specimens S125 t9–S200 t9-S, S125 t9–S200 t9-B, and S125 t7–S200 t9-B failed by core rupture in the first tension loading of the $1.0\Delta_{bm}$ cycle, as illustrated in Figures 11a–c and 12a. The rupture occurred at a core strain ranging from 0.42% to 0.71%. Comparison of the core strain gauge reading, as illustrated in Figure 13a, indicates the presence of stress concentration at the end of the core projection stiffener. The stress concentration was not exhibited in the circular specimens, as illustrated in Figure 13b. Table 5 summarizes the maximum force and core strain before rupture occurred.

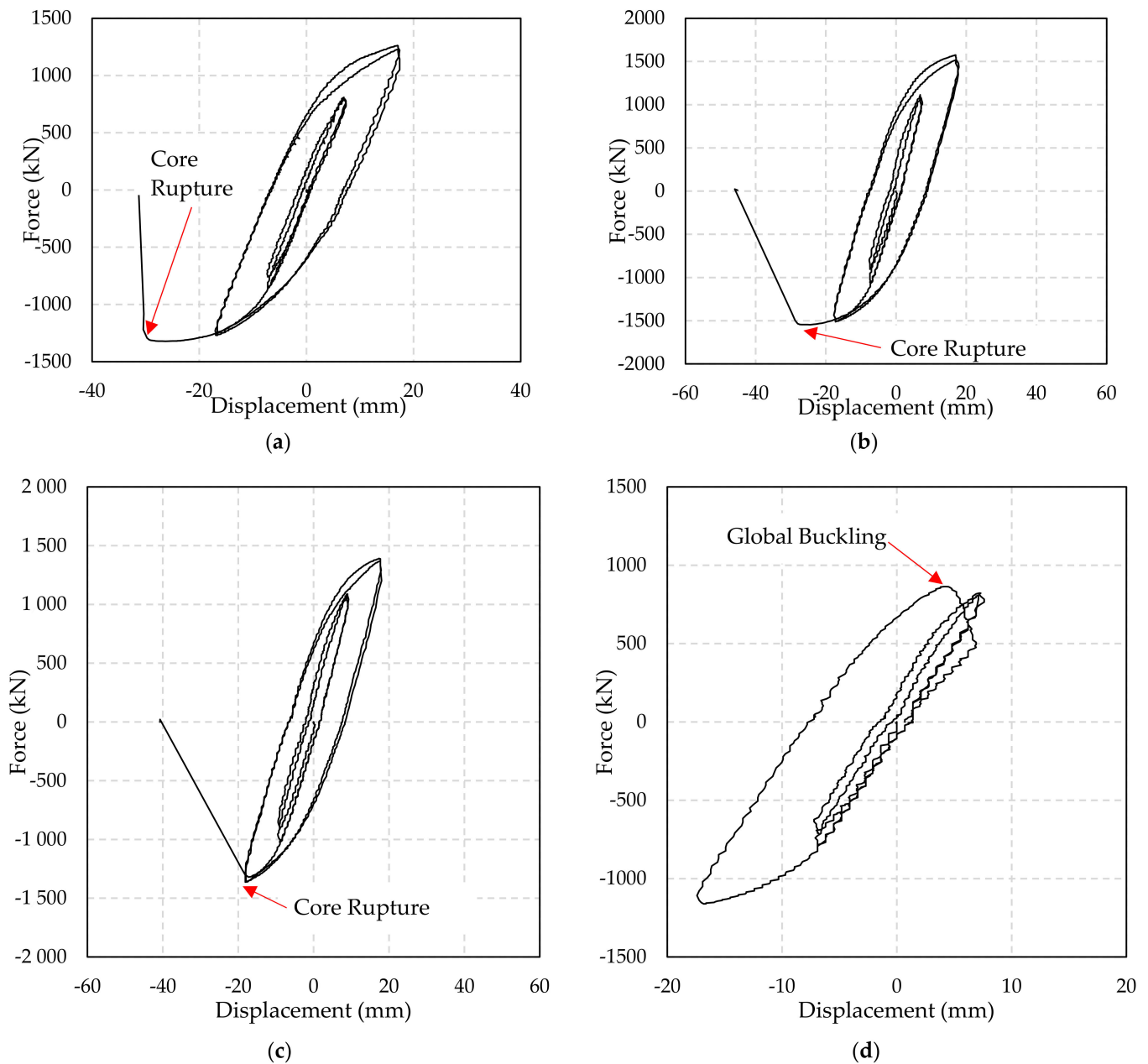


Figure 11. Hysteretic response of circular specimens: (a) *S125 t9–S200 t9-S*; (b) *S125 t9–S200 t9-B*; (c) *S125 t7–S200 t9-B*; (d) *S100 t9–S175 t6-B*.

The square specimen *S100 t9–S175 t6-B*, with P_{cr}/P_y and P_{cy}/P_y ratios of 0.9 and 0.76, respectively, failed by global buckling under a compressive force equal to 77% of P_{cr} . When global buckling occurred, the P_{max}/P_{cy} ratio was 0.92, suggesting that yielding of the casing resulted in global buckling, although the maximum force was lower than P_{cr} .

Figure 13 illustrates the comparison of strain at different core locations in square and circular specimens. Evident from the graphs, the strain at the end of the core projection stiffener was above the strain in the yielding portion of the BRB core, implying the existence of stress concentration. In contrast, stress concentration was not observed in the circular specimens up to core strains four times the core strain at the onset of rupture in square specimens.

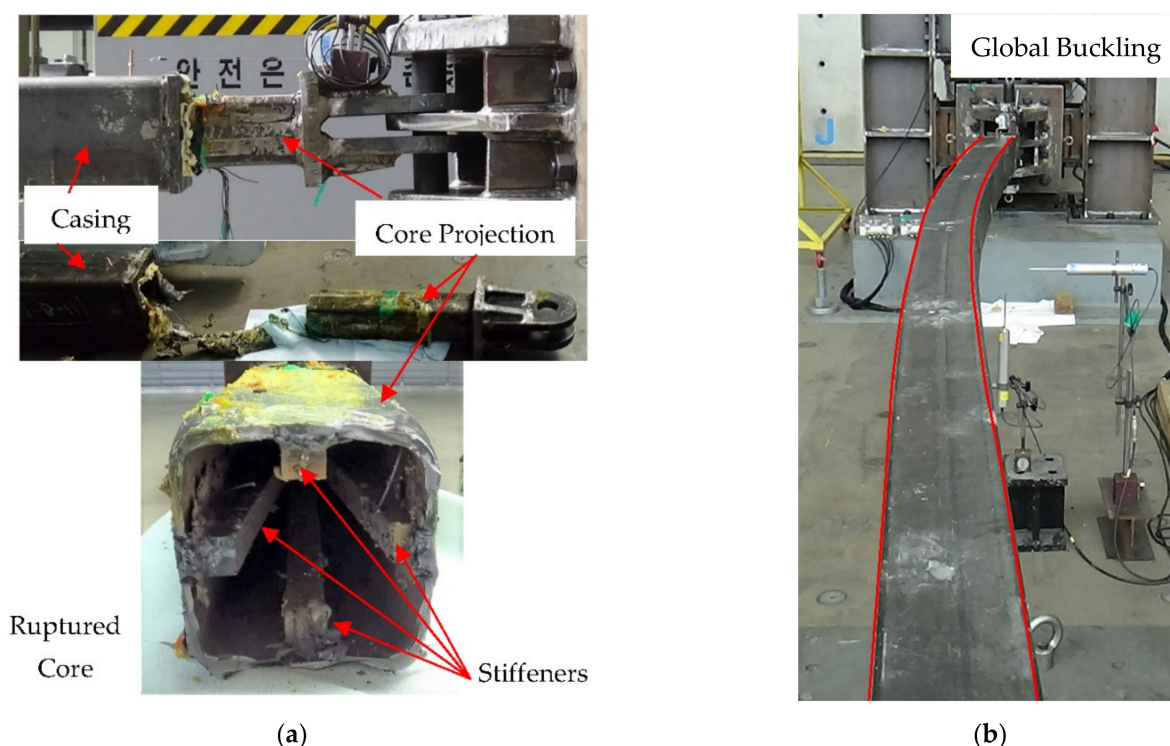


Figure 12. Failure mode of square specimens: (a) Core rupture at the end of unconstrained length stiffener in specimens *S125 t9-S200 t9-S*, *S125 t9-S200 t9-B*, and *S125 t7-S200 t9-B*; (b) global buckling of specimen *S100 t9-S175 t6-B*.

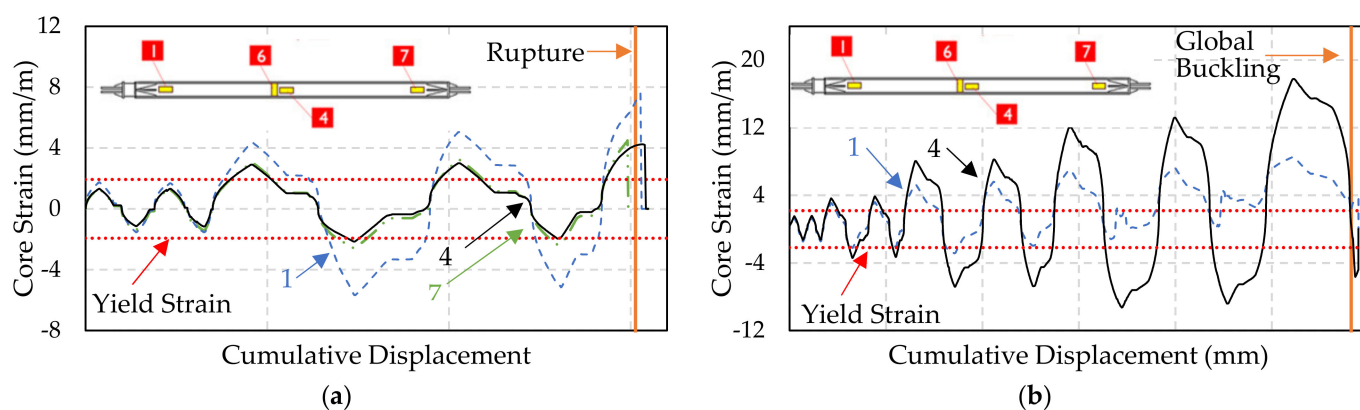


Figure 13. Typical core strain distribution: (a) square specimens; (b) circular specimens.

Table 5. Square specimens test results.

| Specimen | P_{max} (kN) | | δ_{max} (mm) | | ϵ_{max} (%) ³ | | $\frac{P_{max}}{P_{cr}}$ ⁴ | $\frac{P_{max}}{P_{cy}}$ ⁵ | Failure Mode |
|--------------------------|-------------------|-------------------|---------------------|------|-----------------------------------|------|---------------------------------------|---------------------------------------|--|
| | (+) ¹ | (−) ² | (+) | (−) | (+) | (−) | | | |
| <i>S125 t9-S200 t9-S</i> | 1517 ⁶ | 1589 ⁶ | 17.4 | 30.4 | 0.40 | 0.71 | 0.63 | 0.74 | Core rupture at the end of the core projection stiffener |
| <i>S125 t9-S200 t9-B</i> | 1574 | 1546 | 17.9 | 27.4 | 0.42 | 0.64 | 0.65 | 0.77 | |
| <i>S125 t7-S200 t9-B</i> | 1390 | 1362 | 18.0 | 18.1 | 0.42 | 0.42 | 0.58 | 0.68 | |
| <i>S100 t9-S175 t6-B</i> | 863 | 1161 | 7.6 | 17.4 | 0.18 | 0.40 | 0.77 | 0.92 | Global buckling |

¹ Compression. ² Tension. ³ Core strain. ⁴ Maximum compressive force to Euler buckling force ratio. ⁵ Maximum compressive force to casing yield force ratio. ⁶ Brace axial force.

4. Finite Element Analysis

To elucidate the behavior of the proposed BRB, an analytical model of C216 t8–C267 t6-B3 and S125 t9–S200 t9-B was formulated using the finite element program ABAQUS (Dassault Systemes Simulia Corp., Johnston, RI, USA) [30]. The interaction properties and adapted material models are summarized in Table 6. To reflect the cyclic response of the BRB, the material nonlinearity of the steel core and casing was considered using the Chaboche combined isotropic and kinematic hardening model. The Chaboche model parameters were independently calibrated for the square and circular specimens analyzed. The calibrated hardening parameters with three back stresses are listed in Table 7. Material properties of the stiffener and end connectors at the ends of the BRB were modeled using the Von-Mises yield criteria, using stress–strain relations obtained by the coupon test (Table 2). The weld filler material in the core-stiffener slot weld detail illustrated in Figure 2 was modeled as a bilinear material with a yield stress, ultimate stress, and maximum strain of 520 MPa, 580 MPa, and 0.29, respectively. The elastic modulus of steel adopted for all steel and weld components was 200 GPa. The polymer infill was modeled as an elastic material with elastic modulus and Poisson's ratio of 461 MPa and 0.39. The finite element models were meshed using 20-node solid quadratic elements with reduced integration, C3D20R. Interaction between the steel core and filler material was modeled as hard contact, with no penetration in compression and allowing separation in tension. The interface was modeled as frictionless, owing to the presence of a slippery layer of unsolidified polymer on top of the debonding material layer. The interaction between the filler material and the casing was modeled as a tied surface, considering no relative slip was observed. The first buckling mode shape of the brace with 12 mm ($L/500$) amplitude [28] was adopted as an initial geometric imperfection. To replicate the boundary condition in the test, the ends of the BRB were modeled as pin connection with three direction translation restrained. The cyclic load shown in Figure 5 was applied as a displacement-controlled load on the BRB end with core projection. The nonlinear static analysis was conducted using the full Newton method as a solution technique.

Table 6. Material model and interaction properties.

| Component | Material Model | Interaction with Polymer Infill |
|-------------------------------|--|---|
| Core | Chaboche combined isotropic and kinematic hardening | Frictionless hard contact with no penetration |
| Polymer infill | Elastic | - |
| Casing | Chaboche combined isotropic and kinematic hardening | Tie constraint |
| Weld | Bilinear | Frictionless hard contact with no penetration |
| Stiffeners and end connectors | Multilinear kinematic with true stress–true strain relation from coupon test | - |

Table 7. Chaboche model parameters.

| Model | σ_0 (MPa) | C_1 (MPa) | γ_1 | C_2 (MPa) | γ_2 | C_3 (MPa) | γ_3 | Q (MPa) | b |
|--------------------|---------------------|----------------|------------|----------------|------------|----------------|------------|--------------|------|
| C216 t8–C267 t6-B3 | 190 | 64,515 | 680 | 123,830 | 9985 | 940 | 1 | 33.75 | 7.15 |
| S125 t9–S200 t9-B | 230 | 109,347 | 869 | 117,933 | 9985 | 4850 | 1 | 33.75 | 7.15 |

Figure 14 illustrates a comparison of the test and analysis results. As can be observed from the hysteresis response, the cyclic response from the test and analysis are in good agreement. The stress concentration at the end of the core projection stiffener was investigated. Evaluation of core plastic strain (PEEQ) in the square and circular BRB indicated the presence of strain concentration at the end of the stiffener slot weld. While the strain

concentration was localized at the slot weld end in the circular BRB, it resulted in a band of high strain in the square BRB. The plastic strain comparisons are illustrated in Figure 15. From these results, it can be concluded that the adopted stiffener slot welding detail is favorable for the circular BRB core but not for the square BRB core.

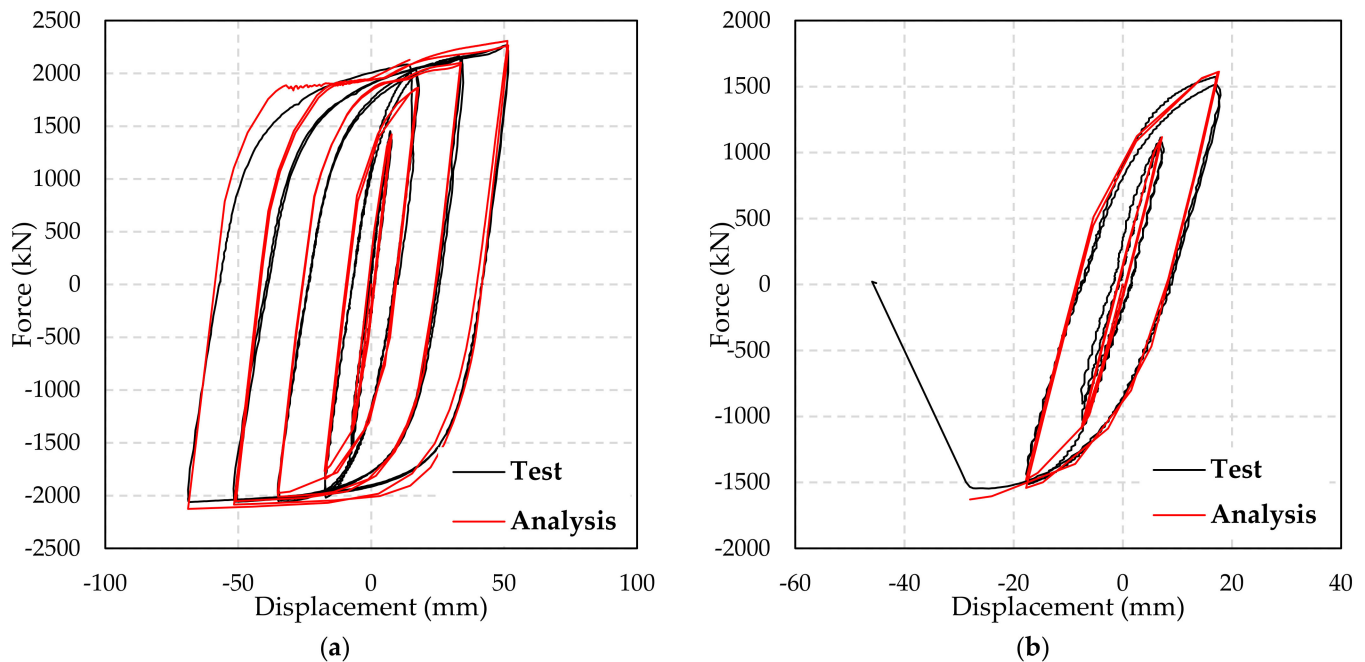


Figure 14. Comparison of finite element and results: (a) C216 t8–C267 t6-B3; (b) S125 t9–S200 t9-B.

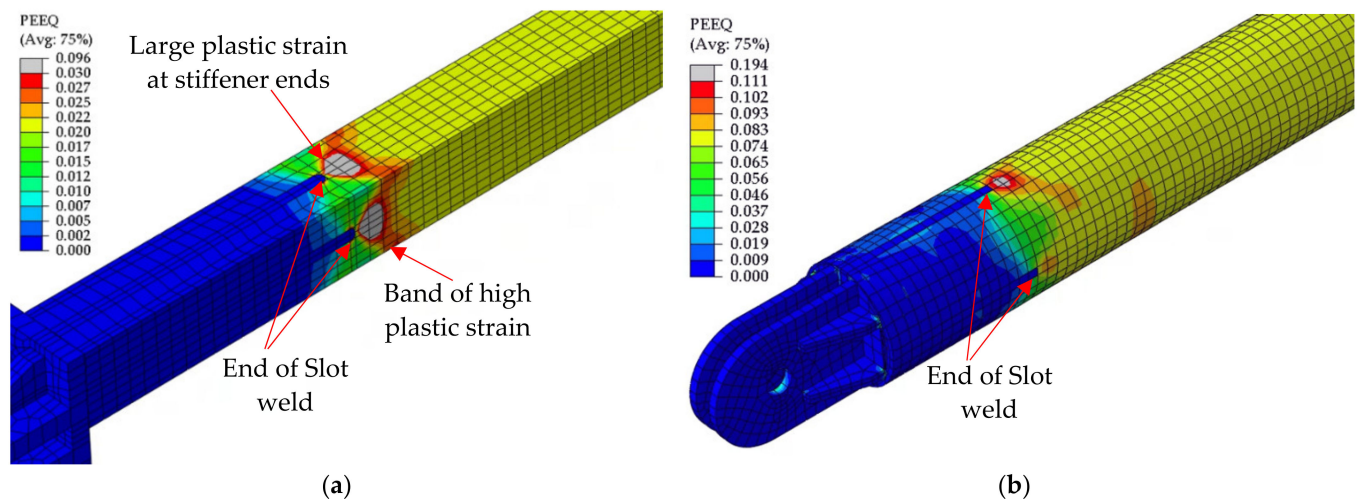


Figure 15. Equivalent plastic strain (PEEQ) distribution: (a) S125 t9–S200 t9-B at $0.5\Delta_{bm}$; (b) C216 t8–C267 t6-B3 at $2.0\Delta_{bm}$.

5. Conclusions

A tube-in-tube BRB with core projection only on one side was developed by restraining circular and square tubes with larger tubes of similar shapes, infilled with lightweight rapid-hardening polymer. Ten full-scale specimens were tested in brace and subassembly test setup, followed by finite element analysis. Circular specimens designed with P_{cr}/P_y , and P_{cy}/P_y ratios of 1.46 and 1.2 exhibited a stable hysteresis response up to 1.42% and 1.06% strain in tension and compression. The maximum compressive load developed was 68% and 82% of P_{cr} and P_{cy} , respectively. Circular specimens designed with P_{cr}/P_y , and P_{cy}/P_y , ranging from 0.82 to 1.06, and 0.7 to 0.87, respectively, and a square specimen designed with P_{cr}/P_y , and P_{cy}/P_y of 0.9 and 0.76 exhibited stable hysteresis before failing

by global buckling, at compressive core strains ranging from 0.18% to 1.10%. Square specimens designed with P_{cr}/P_y and P_{cy}/P_y ranging from 1.39 to 1.50, respectively, failed by core rupture at tensile core strains ranging from 0.42% to 0.71%. Strain gauge readings and finite element analysis results indicated the presence of large plastic strain demand in square specimens because of the stiffener slot weld adopted. The same weld detail did not result in a similar plastic strain demand in the circular specimens. Based on the test results and the finite element analysis, the following conclusions can be drawn:

1. Despite the leakage of unsolidified filler material, the infilled polymer provided sufficient restraint against strength or stiffness degradation due to local or global core deformation, up to a compressive core strain of 1.1%
2. The slot weld detail adopted for welding stiffeners indicated a stable performance, up to a tensile core strain of 1.46% in circular BRBs. However, the slot weld resulted in a band of high plastic strain region in square BRBs, leading to a premature rupture at tensile core strains ranging from 0.42 to 0.71.
3. In circular test specimens with $P_{cr}/P_y = 1.06$ and a square specimen with $P_{cr}/P_y = 0.9$, global buckling occurred at a compressive force equal to 77–82% of the critical buckling force when the casing moment reached 92–100% of the casing yield moment. This indicates that global buckling occurred owing to the yielding of the case, and both the stiffness and strength of the casing should be considered when proportioning a BRB.

Leakage of unsolidified filler material was observed during all the tests. Further research is needed to examine the influence of this phenomenon and investigate possible remedies.

Author Contributions: Conceptualization, R.W.A., Y.K., M.P. and Y.K.J.; methodology, R.W.A., Y.K., M.P. and Y.K.J.; software, R.W.A.; validation, R.W.A., Y.K., M.P., M.J.P. and Y.K.J.; formal analysis, R.W.A.; investigation, R.W.A., Y.K., M.P. and Y.K.J.; resources, Y.K., M.P. and Y.K.J.; data curation, R.W.A.; writing—original draft preparation, R.W.A.; writing—review and editing, R.W.A. and Y.K.J.; visualization, R.W.A., Y.K., M.J.P., M.P. and Y.K.J.; supervision, R.W.A., Y.K., M.J.P., M.P. and Y.K.J.; project administration, Y.K.J.; funding acquisition, Y.K., M.P. and Y.K.J. All authors have read and agreed to the published version of the manuscript.

Funding: This work was supported by the National Research Foundation of Korea (NRF) grant funded by the Korean Government (MSIT) (No. NRF-2020R1A2C3005687) and the Korea Agency for Infrastructure Technology Advancement (KAIA) (21AUDP-B121595-06, 21AUDP-B100343-07).

Institutional Review Board Statement: Not applicable.

Informed Consent Statement: Not applicable.

Data Availability Statement: Data are contained within the article.

Conflicts of Interest: The authors declare no conflict of interest.

References

1. Sabelli, R.; Mahin, S.; Chang, C. Seismic demands on steel braced frame buildings with buckling-restrained braces. *Eng. Struct.* **2003**, *25*, 655–666. [\[CrossRef\]](#)
2. Kiggins, S.; Uang, C.-M. Reducing residual drift of buckling-restrained braced frames as a dual system. *Eng. Struct.* **2006**, *28*, 1525–1532. [\[CrossRef\]](#)
3. Naghavi, M.; Rahnavard, R.; Thomas, R.J.; Malekinejad, M. Numerical evaluation of the hysteretic behavior of concentrically braced frames and buckling restrained brace frame systems. *J. Build. Eng.* **2019**, *22*, 415–428. [\[CrossRef\]](#)
4. Mahrenholtz, C.; Lin, P.-C.; Wu, A.-C.; Tsai, K.-C.; Hwang, S.-J.; Lin, R.-Y.; Bhayusukma, M.Y. Retrofit of reinforced concrete frames with buckling-restrained braces. *Earthq. Eng. Struct. Dyn.* **2015**, *44*, 59–78. [\[CrossRef\]](#)
5. Almeida, A.; Ferreira, R.; Proença, J.; Gago, A. Seismic retrofit of RC building structures with Buckling Restrained Braces. *Eng. Struct.* **2017**, *130*, 14–22. [\[CrossRef\]](#)
6. Shin, J.; Kim, J.; Lee, K. Seismic assessment of damaged piloti-type RC building subjected to successive earthquakes. *Earthq. Eng. Struct. Dyn.* **2014**, *43*, 1603–1619. [\[CrossRef\]](#)
7. Clark, P.W.; Aiken, I.D.; Kasai, K.; Kimura, I. Large-Scale Testing of Steel Unbonded Braces for Energy Dissipation. In Proceedings of the American Society of Civil Engineers Structures Congress 2000, Philadelphia, PA, USA, 8–10 May 2000. [\[CrossRef\]](#)

8. Black, C.J.; Makris, N.; Aiken, I.D. Component Testing, Seismic Evaluation and Characterization of Buckling-Restrained Braces. *J. Struct. Eng.* **2004**, *130*, 880–894. [[CrossRef](#)]
9. Palazzo, G.S.; López-Almansa, F.; Cahís, X.; Crisafulli, F. A low-tech dissipative buckling restrained brace. Design, analysis, production and testing. *Eng. Struct.* **2009**, *31*, 2152–2161. [[CrossRef](#)]
10. Hoveidae, N.; Tremblay, R.; Rafezy, B.; Davaran, A. Numerical investigation of seismic behavior of short-core all-steel buckling restrained braces. *J. Constr. Steel Res.* **2015**, *114*, 89–99. [[CrossRef](#)]
11. Xie, Q. State of the art of buckling-restrained braces in Asia. *J. Constr. Steel Res.* **2005**, *61*, 727–748. [[CrossRef](#)]
12. Hoveidae, N.; Rafezy, B. Overall buckling behavior of all-steel buckling restrained braces. *J. Constr. Steel Res.* **2012**, *79*, 151–158. [[CrossRef](#)]
13. Zhao, J.; Wu, B.; Ou, J. A novel type of angle steel buckling-restrained brace: Cyclic behavior and failure mechanism. *Earthq. Eng. Struct. Dyn.* **2011**, *40*, 1083–1102. [[CrossRef](#)]
14. Alemayehu, R.W.; Kim, Y.; Bae, J.; Ju, Y.K. Cyclic Load Test and Finite Element Analysis of NOVEL Buckling-Restrained Brace. *Materials* **2020**, *13*, 5103. [[CrossRef](#)] [[PubMed](#)]
15. Kim, D.-H.; Lee, C.-H.; Ju, Y.K.; Kim, S.-D. Subassembly test of buckling-restrained braces with H-shaped steel core. *Struct. Des. Tall Spec. Build.* **2014**, *24*, 243–256. [[CrossRef](#)]
16. Wang, C.-L.; Gao, Y.; Cheng, X.; Zeng, B.; Zhao, S. Experimental investigation on H-section buckling-restrained braces with partially restrained flange. *Eng. Struct.* **2019**, *199*, 109584. [[CrossRef](#)]
17. Ryu, J.; Kim, Y.Y.; Park, M.W.; Yoon, S.-W.; Lee, C.-H.; Ju, Y.K. Experimental and numerical investigations of steel-polymer hybrid floor panels subjected to three-point bending. *Eng. Struct.* **2018**, *175*, 467–482. [[CrossRef](#)]
18. Wu, H.; Huang, M.; Li, X.; Xia, Y.; Wang, Z.; Fan, G. Temperature-dependent reversed fracture behavior of multilayered TiBw/Ti–Ti(Al) composites. *Int. J. Plast.* **2021**, *141*, 102998. [[CrossRef](#)]
19. Zhao, J.; Wu, B.; Ou, J. Flexural Demand on Pin-Connected Buckling-Restrained Braces and Design Recommendations. *J. Struct. Eng.* **2012**, *138*, 1398–1415. [[CrossRef](#)]
20. Ju, Y.K.; Kim, M.-H.; Kim, J.; Kim, S.-D. Component tests of buckling-restrained braces with unconstrained length. *Eng. Struct.* **2009**, *31*, 507–516. [[CrossRef](#)]
21. Li, C.; Wang, L.; Weng, Y.; Qin, P.; Li, G. Nonlinear Analysis of Steel Structure Bent Frame Column Bearing Transverse Concentrated Force at the Top in Factory Buildings. *Metals* **2020**, *10*, 1664. [[CrossRef](#)]
22. Flodr, J.; Krejsa, M.; Mikolasek, D.; Sucharda, O.; Židek, L. Mathematical Modelling of Thin-Walled Cold-Rolled Cross-Section. *Appl. Mech. Mater.* **2014**, *617*, 171–174. [[CrossRef](#)]
23. Alemayehu, R.W.; Jung, S.; Bae, J.; Lee, C.-H.; Ju, Y.K. Tapered reduced deep beam connection for long span steel moment frames. *Eng. Struct.* **2021**, *244*, 112731. [[CrossRef](#)]
24. Tsai, K.-C.; Wu, A.-C.; Wei, C.-Y.; Lin, P.-C.; Chuang, M.-C.; Yu, Y.-J. Welded end-slot connection and debonding layers for buckling-restrained braces. *Earthq. Eng. Struct. Dyn.* **2014**, *43*, 1785–1807. [[CrossRef](#)]
25. Pan, W.; Tong, J.; Guo, Y.; Wang, C. Optimal design of steel buckling-restrained braces considering stiffness and strength requirements. *Eng. Struct.* **2020**, *211*, 110437. [[CrossRef](#)]
26. Chou, C.C.; Chen, S.Y. Subassembly tests and finite element analyses of sandwiched buckling-restrained braces. *Eng. Struct.* **2010**, *32*, 2108–2121. [[CrossRef](#)]
27. Watanabe, A.; Hitomi, Y.; Saeki, E.; Wada, A.; Fujimoto, M. Properties of brace encased in buckling-restraining concrete and steel tube. In Proceedings of the 9th World Conference on Earthquake Engineering, Tokyo, Japan, 2–6 August 1988; Volume 4, pp. 719–724.
28. American Institute of Steel Construction (AISC). *Specification for Structural Steel Buildings*; AISC 360-16; American Institute of Steel Construction: Chicago, IL, USA, 2016.
29. American Institute of Steel Construction (AISC). *Seismic Provisions for Structural Steel Buildings*; AISC 341-16; American Institute of Steel Construction: Chicago, IL, USA, 2016.
30. ABAQUS/CAE, version 2017; Software for Technical Computation; Simulia Corp.: Providence, RI, USA, 2017.